

# Ignition and Combustion Characterization of $\text{Ca}(\text{IO}_3)_2$ -based Pyrotechnic Composites with B, Al, and Ti

Haiyang Wang,<sup>[a]</sup> Dylan J. Kline,<sup>[a]</sup> Miles Rehwoldt,<sup>[a]</sup> and Michael R. Zachariah<sup>\*[a]</sup>

**Abstract:** This paper studies the reactive behavior of calcium iodate with Al, B and Ti fuel particles as a thermal and iodine release source for neutralization of biological materials that might be employed in weapons. Two different calcium iodate particle length scales (micron and submicron) with different fuel/oxidizer ratios were used to prepare the iodized nanopyrolants. The optimal ratio was found to be the one with equivalence ratio of 2.0 for all the three fuels. The reactivity of the pyrolants can be enhanced by dehydrating the  $\text{Ca}(\text{IO}_3)_2$  or replacing the micron oxidizer particles with submicron particles. The thermal decomposition process of the pyrolants was investigated at low and high

heating rate. The results show that B, Al and Ti nanoparticles can promote the decomposition of  $\text{Ca}(\text{IO}_3)_2$ , but the Ti nanoparticles are the most efficient, which lower temperature of the oxygen/iodine release from  $\sim 660^\circ\text{C}$  to  $\sim 400^\circ\text{C}$ . Thus,  $\text{Ti}/\text{Ca}(\text{IO}_3)_2$  has the lowest ignition temperature of  $\sim 400^\circ\text{C}$ . The various calcium iodate-based pyrolants were shown to have a wide range of reactivity (1–4 orders of magnitude) and burn times (1–3 orders of magnitude), high flame temperature (1850–2800 K) and iodine loading capacity ( $\sim 20$ –60 wt.-% of iodine), which makes it a promising class of biocidal energetic materials.

**Keywords:** Calcium iodate · aluminum · boron · titanium · iodine


## 1 Introduction

Despite the Geneva Convention 1972 ban on biological weapons, these materials are of significant concern [1]. Methods to neutralize these materials through application of intense heat pulses are in some cases though to be insufficient, and methods that combine both heat and a chemical effect are under serious consideration. One such chemical effect is through the use of iodine as a biocidal remnant produced following the thermal pulse [2–7]. Another possible application of these iodized energetic materials is served as an efficient iodine supply system for a Chemical Oxygen Iodine Laser (COIL) system [8]. Both elemental iodine and iodine compounds have been incorporated into the formulas of energetic materials [9–12]. However, direct addition of elemental iodine reduces the thermal output of the formulation because iodine is a passive agent [9]. In order to maintain high reactivity without compromising iodine content, different iodine-containing oxidizers such as  $\text{I}_2\text{O}_5$ ,  $\text{AgIO}_3$ ,  $\text{Ca}(\text{IO}_3)_2$ ,  $\text{Cu}(\text{IO}_3)_2$ ,  $\text{Fe}(\text{IO}_3)_3$  and  $\text{Bi}(\text{IO}_3)_3$  have been explored [3, 13–18]. In addition, to their high iodine content, these oxidizers have a high enthalpy of reaction and high flame temperature when used as part of an Al-based pyrolant mixture (Table S1). Notably,  $\text{Al}/\text{I}_2\text{O}_5$  has the highest iodine content (67 wt.-%) and a high reactivity [19, 20]. However, the hygroscopic nature of  $\text{I}_2\text{O}_5$  can negatively impacting reactivity. For  $\text{Al}/\text{AgIO}_3$ , it has been shown that most of the iodine favors the formation of AgI instead of  $\text{I}_2$ , thus reducing the biocidal impact [21].  $\text{Al}/\text{Cu}(\text{IO}_3)_2$ ,  $\text{Al}/\text{Fe}(\text{IO}_3)_3$  and  $\text{Al}/\text{Bi}(\text{IO}_3)_3$  composites were also found to de-

stroy bacterial spores efficiently [22], but the amount of iodine released may be reduced as a result of reactions of iodine gas with Cu, Fe, and Bi [3]. Recently,  $\text{Ca}(\text{IO}_3)_2$  was found to be an alternative to release iodine efficiently when reacting with aluminum and boron [3, 13, 14, 18], however, the ignition and combustion characterization of  $\text{Ca}(\text{IO}_3)_2$ -based pyrolants have not been systematically investigated.

In this paper,  $\text{Ca}(\text{IO}_3)_2$  particles (containing crystal water) with two different size distributions were incorporated with the three different reactive fuels of aluminum (Al), boron (B) and titanium (Ti) to form powder composites using a conventional physical mixing method. Different composites with various fuel (Al, B, and Ti) to oxidizer ( $\text{Ca}(\text{IO}_3)_2$ , with crystal water) ratios from fuel lean to fuel rich were prepared and the combustion characterizations of peak pressure, pressure rise rate, and burning time were systematically investigated and reported. By varying the fuels and the size of the oxidizer, the peak pressure, the pressure rise rate, and the burn time can easily be adjusted. Most importantly, the iodine content of the composites can be varied from  $\sim 20$  to  $\sim 60$  wt.-% with a high flame temperature. The ignition temperatures of  $\text{Al}/\text{Ca}(\text{IO}_3)_2$ ,  $\text{B}/\text{Ca}(\text{IO}_3)_2$ , and  $\text{Ti}/\text{Ca}(\text{IO}_3)_2$

[a] H. Wang, D. J. Kline, M. Rehwoldt, M. R. Zachariah  
Department of Chemical and Biomolecular Engineering and Department of Chemistry and Biochemistry, University of Maryland College Park, Maryland, 20742, United States of America  
\*e-mail: mrz@umd.edu

 Supporting information for this article is available on the WWW under <https://doi.org/10.1002/prop.201800041>

were measured and the primary product species ( $O_2$  and  $I_2$ ) characterized in slow and high heating rates. These results systematically reveal the ignition/combustion properties and iodine release performance of the calcium iodate based pyrolants and should eventually enlarge the application range of this class of energetic materials.

## 2 Experimental Section

### 2.1 Chemicals

Boron nanoparticles (NPs, SB99, ~62 nm, ~65 wt-% active boron) were obtained from the SB Boron Corporation, Al nanoparticles (Al NPs, ~85 nm, 81 wt-% active Al) were purchased from Novacentrix, and titanium nanoparticles (Ti NPs, ~50 nm, 75 wt-% active Ti) were purchased from US Research Nanomaterials, Inc. The active content of the three fuels was confirmed by thermogravimetric analysis (TGA).  $Ca(NO_3)_2 \cdot 4H_2O$  ( $\geq 99.0\%$ ) and  $KIO_3$  (99.5%) were purchased from Sigma-Aldrich.  $Al_2O_3$  (~25 nm,  $\gamma$ -phase),  $TiO_2$  (~25 nm, anatase) and  $H_3BO_3$  (commercial, large crystals) are purchased from Sigma-Aldrich. All the above chemicals were used as received. Deionized (DI) water was produced using a water purification system purchased from ELGA (Model: LA621).

### 2.2 Preparation of Large and Sub-micron $Ca(IO_3)_2$ Particles by Ball Milling

The detailed information of ball milled formation of  $Ca(IO_3)_2$  can be found in ref. [13]. Generally, 236 mg  $Ca(NO_3)_2 \cdot 4H_2O$  and 428 mg  $KIO_3$  were dry ball-milled for 30 min with 3 milling balls (ball-to-material ratio is 1.80), and the product  $Ca(IO_3)_2$  particles recovered after washing with DI water to remove the  $KNO_3$ . When milled, with alumina balls (ball-to-material ratio is 1.80) the resulting average particle size of ~2  $\mu m$  (0.5–6.5  $\mu m$ , Figure S1a) was obtained. With hardened steel balls (ball-to-material ratio is 6.14) the particles had an average size of ~200 nm (Figure S1b). The size distribution and average size was obtained by measuring at least 200 particles on the SEM images (nano Measurer 1.2). All  $Ca(IO_3)_2$  particles used in this paper are hydrated unless noted otherwise.

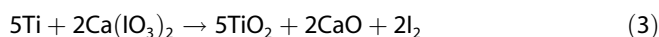
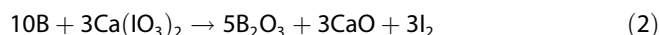
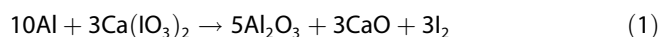
### 2.3 TG/MS, SEM/EDS, XRD

Thermogravimetric/mass spectrum (TG/MS) results were obtained with a TA Instruments Q600 at a rate of  $10^\circ C/min$  up to  $1000^\circ C$  in an Ar atmosphere (100 mL/min). A Hitachi Su-70 scanning electron microscope attached with energy-dispersive X-ray spectroscopy (SEM/EDS) was used to analyze the particle size/morphology and elemental composition, respectively. The obtained  $Ca(IO_3)_2$  particles were attached

to the SEM stage using carbon tape. A Bruker X-ray diffractometer (XRD, D8 with  $Cu K_\alpha$  radiation) was used to determine the crystallinity state of the  $Ca(IO_3)_2$ .

### 2.4 Preparation of Pyrolant Composites

The pyrolant composites were prepared by a conventional physical mixing method. A total mass of 150 mg of each sample was prepared and added to a vial with 10 mL hexane. After 30 minutes of sonication, the uncovered vial was placed in a fume hood overnight to dry and then broken gently with a spatula. The active contents of boron (~65%), aluminum (~81%) and titanium (~75%) were taken into consideration when calculating the equivalence ratio as follows (dehydrated calcium iodate):



The detailed formula of the pyrolant composite particles with different equivalence ratios in this study was shown in Table S2, which also includes the corresponding mass and mass percentage of the fuel and oxidizer.

### 2.5 T-Jump Ignition and Time-Resolved Mass Spectrometry

The details of T-jump mass spectrometry (T-Jump MS) method to determine ignition temperature and the temporal evolution of species can be found in ref. [23]. The schematic showing of T-Jump MS can be found in Figure S2a. Typically, a ~10 mm long platinum filament (~76  $\mu m$  in diameter) coated with the pyrolant composites (~4 mm long) was resistively heated to ~1400 K (heating rate of  $\sim 4 \times 10^5 K \cdot s^{-1}$ , in 1 atm of Argon). The ignition and subsequent combustion of the composite was monitored using a high-speed camera (14.9  $\mu s$  per frame with  $256 \times 256$  pixels, Phantom V12.1). The temporal wire resistance (correlated to temperature) during the heating process was recorded and the ignition temperature was calculated by correlating the observed ignition timestamp from the high-speed video with the wire temperature profile [23]. A high speed, time-of-flight mass spectrometer was also coupled with the ignition filament, which is used for detecting the species released during fast heating.

### 2.6 Combustion Cell and Flame Temperature Measurements

The pyrolant composites were evaluated in a constant volume (~20  $cm^3$ ) combustion cell, from which the peak pres-

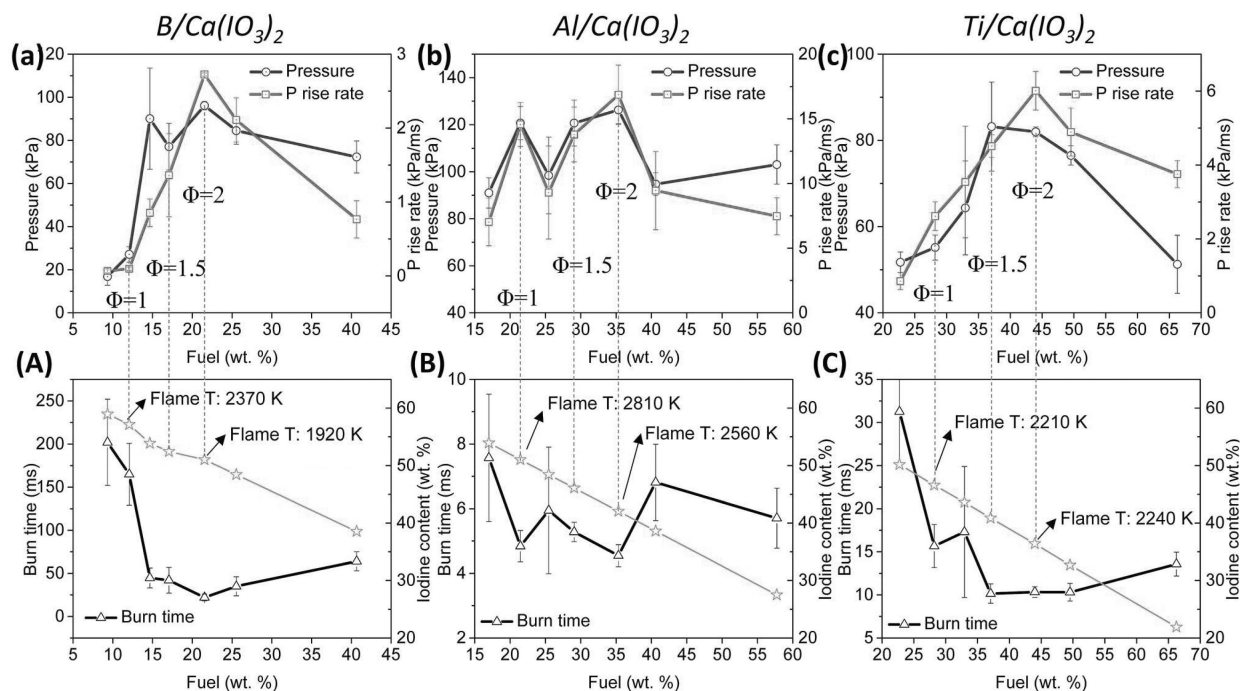


**Figure 1.** Peak pressure (a–c), pressure rise rate (a–c), burn time (A–C) and iodine content (A–C) of  $\text{B}/\text{Ca}(\text{IO}_3)_2$  (a and A),  $\text{Al}/\text{Ca}(\text{IO}_3)_2$  (b and B) and  $\text{Ti}/\text{Ca}(\text{IO}_3)_2$  (c and C) composites with large  $\text{Ca}(\text{IO}_3)_2$  (different weight percentage of the fuel). The insert numbers are average flame temperatures (in Kelvin) of  $\text{B}/\text{Ca}(\text{IO}_3)_2$ ,  $\text{Al}/\text{Ca}(\text{IO}_3)_2$  and  $\text{Ti}/\text{Ca}(\text{IO}_3)_2$  composites with large hydrated  $\text{Ca}(\text{IO}_3)_2$  (in equivalence ratio of  $\varphi=1$  and  $\varphi=2$ ).

sure, pressure rise rate and burning time (half width of optical curve) were measured and calculated. The details can be found in our previous study [24]. The schematic showing of combustion cell and flame temperature measurement can be found in Figure S2b. The sample mass was  $\sim 25$  mg, and the measurements were replicated in triplicates. The combustion cell experiment was also used for flame temperature measurements. The emission from the combustion event was detected by an optical fiber and sent to a 0.5 m spectrometer (Acton SP500i, 150grooves/mm grating). The spectrum was recorded by a 32 channel PMT (Hamamatsu) coupled with a high-speed data acquisition system (Vertilon IQSP 580). The time resolved spectra (500–800 nm band, 10 kHz) was then fit to Planck’s law with a grey body approximation to get a time-resolved temperature profile [25]. Furthermore, channels that were sensitive to the absorption of light by  $\text{I}_2$  gas were excluded from calculation. The average flame temperature of the combustion events is reported below and in supporting information.

### 3 Results and Discussion

$\text{Ca}(\text{IO}_3)_2$  particles with an average size of  $\sim 2$   $\mu\text{m}$  were prepared by a facile ball milling process and different  $\text{B}/\text{Ca}(\text{IO}_3)_2$ ,  $\text{Al}/\text{Ca}(\text{IO}_3)_2$ , and  $\text{Ti}/\text{Ca}(\text{IO}_3)_2$  pyrolants from fuel lean to fuel rich (equivalence ratio: 0.75–5.0) were prepared by a

conventional physical mixing method. The detailed formulations and typical SEM images of these composites are shown in Table S2 and Figure S3, respectively. The SEM images indicate close contact between the fuel (B, Al and Ti) and oxidizer (calcium iodate), however, the images also show a high degree of particle size variability (fuel:  $< 100$  nm, oxidizer: 2000 nm) and low interfacial area, likely due to the large size of  $\text{Ca}(\text{IO}_3)_2$  particles. The reactivity of the pyrolant composites was evaluated by a confined combustion cell ( $\sim 20$  mL) where the peak pressure, pressure rise rate and burn time was obtained. Three experiments were conducted for each sample and the average values with standard error bar were reported and shown in Figure 1. Although the peak pressure and pressure rise rate fluctuate slightly between 1.0 and 1.5, an increase in fuel content corresponds to trends which are increasing until peaking at an equivalence ratio of 2.0 for all three pyrolant types. Since the combustion cell experiments were conducted in air, it is natural that fuel-rich pyrolants are more reactive. Interestingly, the optimal equivalence ratio was 2.0, which is markedly higher than expected ( $\sim 1.1$ – $1.5$ ) [25,26] and suggests other factors impacting combustion that will be discussed in a later section. Among these three pyrolants, B- and Ti-based composites are more sensitive to the equivalence ratio, with peak pressure  $\sim 4$  times (Figure 1a) and  $\sim 1.5$  times (Figure 1c) higher, and the pressure rise rates  $\sim 27$  times (Figure 1a) and  $\sim 2.3$  times (Figure 1c) higher when the

equivalence ratio is increased from 1 to 2. However, in the case of Al-based composites (Figure 1b), the peak pressure and pressure rise rate only increased slightly. The burn time of the different pyrolants is shown in Figure 1A–1C to be inversely correlated with pressure rise rate. Among the three fuels (B, Al and Ti), we can see that the Al-based mixture is the most reactive, followed by Ti-based and B-based pyrolants. Correspondingly, the burn time of Al/Ca(IO<sub>3</sub>)<sub>2</sub> is ~4–8 ms while the burn time of B/Ca(IO<sub>3</sub>)<sub>2</sub> is ~25–250 ms. For some applications, high reactivity is desired in pyrolants for their potential for high dynamic pressures and temperatures. On the other hand, longer burn time means longer exposure and disinfecting time, which could also be required in sporicides. Here, different Ca(IO<sub>3</sub>)<sub>2</sub>-based pyrolants with different fuels of B, Al and Ti provide a wide range of reactivity and burn time, demonstrating its application potential in varying conditions.

The iodine content in different pyrolant composites was also calculated and shown in Figure 1A–1C (star markers). As we see in the figures, the iodine content decreases with the increase of fuel content in the pyrolants. The iodine content of different pyrolants of B/Ca(IO<sub>3</sub>)<sub>2</sub>, Al/Ca(IO<sub>3</sub>)<sub>2</sub> and Ti/Ca(IO<sub>3</sub>)<sub>2</sub> composites varies in the range of ~40–60 wt.-%, ~30–55 wt.-% and ~20–50 wt.-%, respectively, due to different equivalence ratios, molecular weights and final valence states across different fuels. The flame temperatures of different pyrolants with equivalence ratio of 1.0 and 2.0 were also obtained and shown in Table S3. Exemplary VIS spectra of Al/Ca(IO<sub>3</sub>)<sub>2</sub> and Ti/Ca(IO<sub>3</sub>)<sub>2</sub> reactions and estimated flame temperatures for each reaction were shown in Figure S4. As we see in the Figure 1A–1C and Table S3, the flame temperatures of all the cases with stoichiometric ratio are  $\geq$  ~2200 K. It is not surprising that Al based pyrolant has the highest flame temperature of ~2810 K due to its high reactivity and energy released per mole of Al. However, when the fuel content in the pyrolant composite goes higher (from  $\varphi=1$  to  $\varphi=2$ ), the flame temperatures of the B/Ca(IO<sub>3</sub>)<sub>2</sub> and Al/Ca(IO<sub>3</sub>)<sub>2</sub> were reduced by ~450 and ~250 °C, respectively, while the Ti/Ca(IO<sub>3</sub>)<sub>2</sub> kept the same value.

As mentioned above, the optimal ratio of the fuel and oxidizer in the calcium iodate-based pyrolants is ~2.0 regardless of the fuel composition, which is higher than expected. As we know, B, Al and Ti may react with water during the pyrolant reaction. We believe that this deviation can be attributed to the crystal water inside the Ca(IO<sub>3</sub>)<sub>2</sub>. To investigate this, the calcium iodate particles (~2  $\mu$ m) prepared by ball milling were baked at a temperature of ~350 °C for ~40 min to remove the crystal water. The SEM images and XRD results of the prepared Ca(IO<sub>3</sub>)<sub>2</sub> before and after dehydration are shown in Figure S5a/S5b and Figure S5d/S5e, respectively. The XRD results (Figure S5d and S5e) confirm that the Ca(IO<sub>3</sub>)<sub>2</sub> before heating has one molecule of water which was removed after heating. The SEM images indicate porous inner structure (Figure S5b-1, with a pore size of ~100–300 nm) in the Ca(IO<sub>3</sub>)<sub>2</sub> particles after dehydration, probably because of water evaporation. The

high-resolution SEM image of Ti/Ca(IO<sub>3</sub>)<sub>2</sub> (Figure S5c) with hydrated Ca(IO<sub>3</sub>)<sub>2</sub> indicates that some of the Ti nanoparticles were imbedded into the porous structure.

The reactivity of the dehydrated Ca(IO<sub>3</sub>)<sub>2</sub> composite pyrolants was also evaluated in the combustion cell with the results shown in Figure 2. Both the peak pressure and pressure rise rate of Al/Ca(IO<sub>3</sub>)<sub>2</sub> (dehydrated, Figure 2a) and Ti/Ca(IO<sub>3</sub>)<sub>2</sub> (dehydrated, Figure 2c) peak at the equivalence ratio of 1.5 and 1.0, respectively. This was further confirmed with similar trends in burn time (Figure 2b and 2d) since Al/Ca(IO<sub>3</sub>)<sub>2</sub> and Ti/Ca(IO<sub>3</sub>)<sub>2</sub> have the shortest burn time when the equivalence ratio is 1.5 and 1.0, respectively. When the equivalence ratio further increases to 2.0, the reactivity of both pyrolants decreases and the burn time increases. We conclude that crystal water reacts with the excess fuel, raising the pressure and pressure rise rate of the pyrolant ( $\varphi=2.0$ ) compared to the stoichiometric one (as Figure 1 shows). However, for the cases of B/Ca(IO<sub>3</sub>)<sub>2</sub> and Al/Ca(IO<sub>3</sub>)<sub>2</sub> (hydrated), the flame temperatures of the fuel rich composites ( $\varphi=2.0$ ) are lower, which might be owing to the lesser energy release from fuel-water reaction compared to fuel-Ca(IO<sub>3</sub>)<sub>2</sub> reaction [13,27]. It is also not surprising that all the dehydrated Ca(IO<sub>3</sub>)<sub>2</sub> pyrolants are more reactive compared to those with crystal water in the same equivalence ratio (compare Figure 1 and Figure 2) because of the higher surface area and higher interfacial contact between the fuel and oxidizer.

As the SEM (Figure S3) shows, the contact between the fuel nanoparticles and oxidizers was highly limited due to the large size of Ca(IO<sub>3</sub>)<sub>2</sub> particles. Via mechanochemistry [13,22], we produced Ca(IO<sub>3</sub>)<sub>2</sub> submicron particles with an average diameter of ~200 nm (Figure S1b). The particles were then physically mixed with different fuels of B, Al and Ti and different composite pyrolant particles were obtained. The SEM images are shown in Figure S6, which indicate close contact between the fuel and oxidizer. The reactivity of the composite pyrolant particles was also evaluated in the combustion cell and the results are shown in Figure 3 (summarized in Table S4). These results clearly illustrate an inverse relationship between reactivity of the composite, and size of the Ca(IO<sub>3</sub>)<sub>2</sub> crystals. For example, the pressure and pressure rise rate of Al/Ca(IO<sub>3</sub>)<sub>2</sub> (small) is ~2.5 and ~19 times higher than that with large Ca(IO<sub>3</sub>)<sub>2</sub>, while the burn time is ~3 times shorter. The employment of small Ca(IO<sub>3</sub>)<sub>2</sub> largely enhances the reactivity of the composite pyrolant particles and will eventually extend the range of its application. To demonstrate varied reactivity and iodine release of different pyrolants, 10 mg of B/Ca(IO<sub>3</sub>)<sub>2</sub>, Al/Ca(IO<sub>3</sub>)<sub>2</sub> and Ti/Ca(IO<sub>3</sub>)<sub>2</sub> composites with large ( $\varphi=0.75$  and 2.0) and small ( $\varphi=2.0$ ) crystals were also ignited in air with the combustion events recorded and shown in the supporting information (**Appendix B. supporting videos**).

The ignition properties of the pyrolant composites (with submicron Ca(IO<sub>3</sub>)<sub>2</sub>) were also investigated on a fast-heating Pt wire (heating rate:  $\sim 4 \times 10^5$  K/s and the corresponding high-speed burning snapshots are shown in Figure 4. From

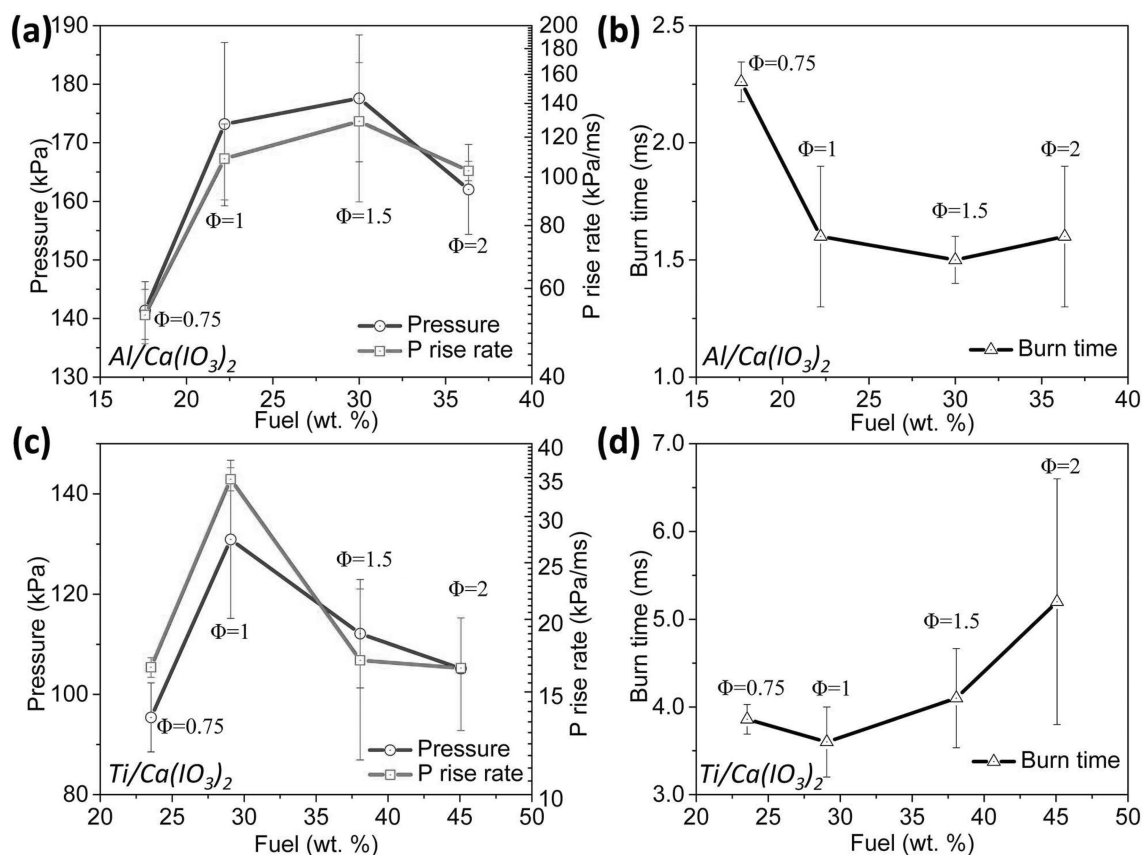


**Figure 2.** Peak pressure (round mark, a and c), pressure rise rate (square mark, a and c), burn time (triangle mark, b and d) of  $\text{Al}/\text{Ca}(\text{IO}_3)_2$  (a and b) and  $\text{Ti}/\text{Ca}(\text{IO}_3)_2$  (c and d) composites with dehydrated  $\text{Ca}(\text{IO}_3)_2$ . (different weight percentage of the fuel).

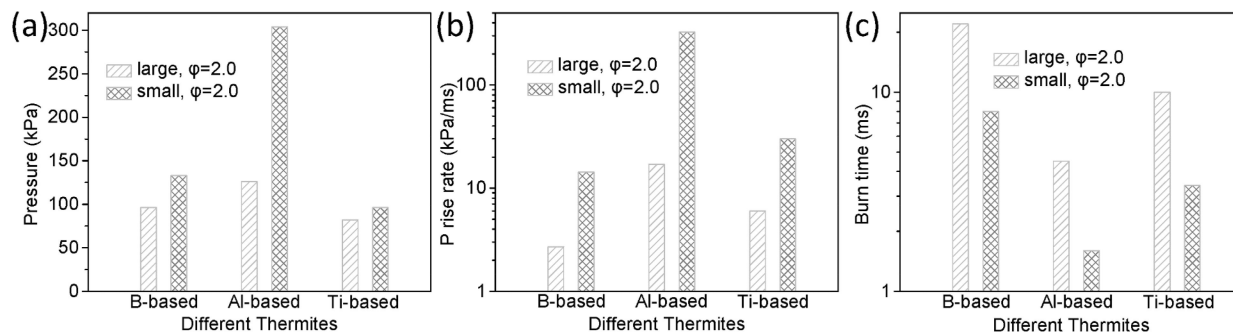


**Figure 3.** Peak pressure (a), pressure rise rate (b), burn time (c) of  $\text{B}/\text{Ca}(\text{IO}_3)_2$ ,  $\text{Al}/\text{Ca}(\text{IO}_3)_2$  and  $\text{Ti}/\text{Ca}(\text{IO}_3)_2$  composites with large and small hydrated  $\text{Ca}(\text{IO}_3)_2$  particles ( $\varphi=2.0$ ).

the images, we can see the light emanated by the  $\text{Al}/\text{Ca}(\text{IO}_3)_2$  is the brightest, followed by  $\text{Ti}/\text{Ca}(\text{IO}_3)_2$  and  $\text{B}/\text{Ca}(\text{IO}_3)_2$ , which is consistent with the observed reactivity within the combustion cell. During the heating pulse ( $\sim 3$  ms), the temperature profile of the wire was recorded and compared with the ignition time (time of first light) in the high-speed video in order to determine the ignition temperature. The ignition temperature of  $\text{B}/\text{Ca}(\text{IO}_3)_2$  and  $\text{Al}/\text{Ca}(\text{IO}_3)_2$  is  $\sim 600^\circ\text{C}$  and  $\sim 650^\circ\text{C}$ , respectively, while the igni-

tion temperature of  $\text{Ti}/\text{Ca}(\text{IO}_3)_2$  is  $\sim 200^\circ\text{C}$  lower. The ignition of  $\text{Al}/\text{Ca}(\text{IO}_3)_2$  and  $\text{B}/\text{Ca}(\text{IO}_3)_2$  might be limited by the melting point of Al ( $660^\circ\text{C}$ ) and the low diffusion rate of oxygen through liquid  $\text{B}_2\text{O}_3$  layer (melts at  $\sim 510^\circ\text{C}$ ) on B. However, since Ti nanoparticles can be ignited  $\sim 300^\circ\text{C}$  in air, the ignition of  $\text{Ti}/\text{Ca}(\text{IO}_3)_2$  might be limited by the decomposition of the oxidizer.

The decomposition process of  $\text{Ca}(\text{IO}_3)_2$  and the related pyrolant composites were investigated separately by slow



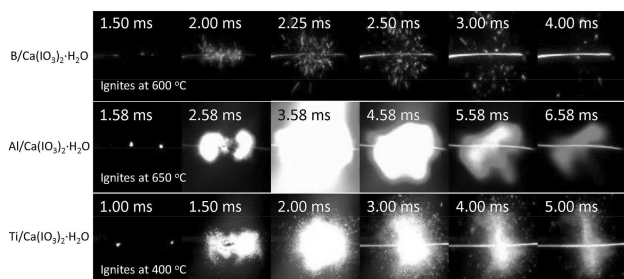


**Figure 4.** High-speed snapshots of B/Ca(IO<sub>3</sub>)<sub>2</sub>, Al/Ca(IO<sub>3</sub>)<sub>2</sub> and Ti/Ca(IO<sub>3</sub>)<sub>2</sub> composites with sub-micron and hydrated Ca(IO<sub>3</sub>)<sub>2</sub> ( $\varphi = 2.0$ ). Labeled are the time (in ms) after triggering and the temperature (°C) when sample ignites.

heating TG/DSC (10 °C/min) and high heating T-Jump MS ( $4 \times 10^5$  K/s). The TG/MS results of different Ca(IO<sub>3</sub>)<sub>2</sub>-based mixtures are shown in Figure 5. The TG curve of hydrated Ca(IO<sub>3</sub>)<sub>2</sub> reveals that the decomposition has three steps (Figure 5a). Initially, the one molecule crystal water was removed at ~220 °C with a ~4.4 wt-% of weight loss, which is consistent with the theoretical value. The decomposition at ~620–660 °C with a weight loss of ~60 wt-% is the major step followed by a minor decomposition at ~660–730 °C with a weight loss of ~20 wt-%. Based on the weight loss data, the probable intermediate product formed (solid) after the second major step is Ca<sub>5</sub>(IO<sub>6</sub>)<sub>2</sub> [28], which then decompose to CaO. The iodine release detected by MS in Fig-

ure 5b also shows a major and minor iodine peak at ~660 and 730 °C, respectively, which further confirms that. Interestingly, Al/Ca(IO<sub>3</sub>)<sub>2</sub> also clearly shows three step decompositions while the Ti/Ca(IO<sub>3</sub>)<sub>2</sub> and B/Ca(IO<sub>3</sub>)<sub>2</sub> cases do not (as confirmed by MS results in Figure 5b).

As Figure 5a and 5b show, compared to pure Ca(IO<sub>3</sub>)<sub>2</sub>, all the fuel containing composites decompose much earlier. Both Al/Ca(IO<sub>3</sub>)<sub>2</sub> and B/Ca(IO<sub>3</sub>)<sub>2</sub> start to decompose ~520 °C, which is ~100 °C lower than the ignition temperature (labeled in Figure 4). However, the ignition of Al/Ca(IO<sub>3</sub>)<sub>2</sub> only occurs when the temperature goes  $\geq 650$  °C, which is  $>100$  °C higher than the decomposition temperature (~520 °C). This indicates the ignition might be limited by the melting of Al (660 °C). In the case of boron, the oxide layer (B<sub>2</sub>O<sub>3</sub>) has a lower melting point (~450 °C), however, once the it melts, it covers the surface and inhibits diffusion of oxygen into it. Therefore, ignition happened at a higher temperature (~600 °C) and, upon formation of CaO (Figure 5a), reactions with B<sub>2</sub>O<sub>3</sub> weaken the shell and allow oxygen diffusion to the fuel. It is evident in the EDS results in Figure S7 that the combustion residue is a homogenous mixture of CaO and B<sub>2</sub>O<sub>3</sub>, although XRD only reveals an amorphous residue. Among the pyrolant mixtures, the Ti/Ca(IO<sub>3</sub>)<sub>2</sub> was the earliest to decompose at ~400 °C, the same temperature at which Ti/Ca(IO<sub>3</sub>)<sub>2</sub> was measured to ignite. Since Ti nanoparticles can be ignited in air at ~300 °C [29], it is supposed that the ignition of Ti/Ca(IO<sub>3</sub>)<sub>2</sub> is limited by the decomposition temperature of Ca(IO<sub>3</sub>)<sub>2</sub>.

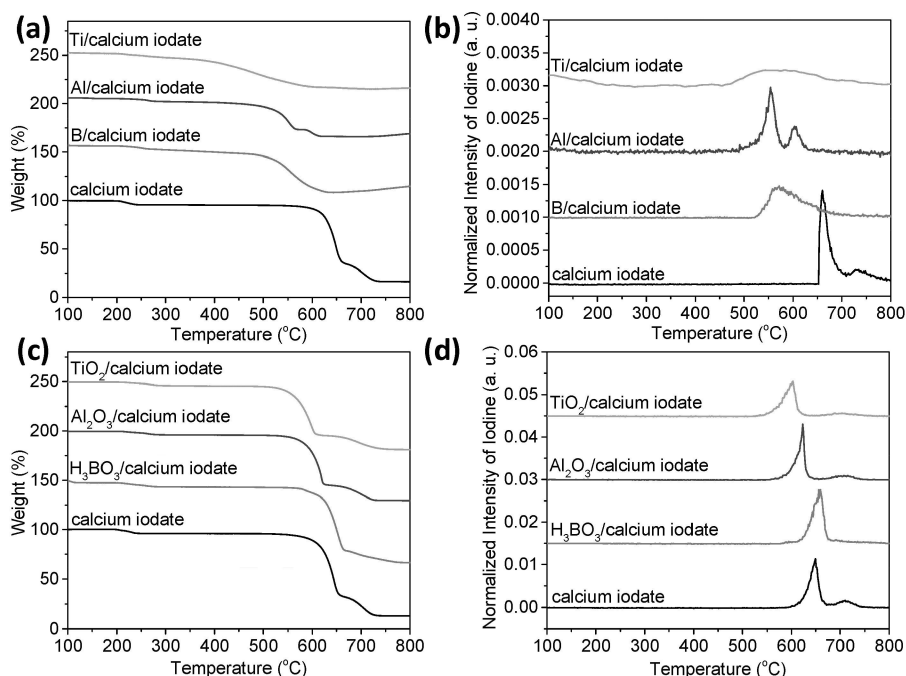


**Figure 5.** TG (a and c)/MS (b and d) results of (a and b) Ca(IO<sub>3</sub>)<sub>2</sub>, B/Ca(IO<sub>3</sub>)<sub>2</sub>, Al/Ca(IO<sub>3</sub>)<sub>2</sub>, Ti/Ca(IO<sub>3</sub>)<sub>2</sub> and (c and d) Ca(IO<sub>3</sub>)<sub>2</sub>, H<sub>3</sub>BO<sub>3</sub>/Ca(IO<sub>3</sub>)<sub>2</sub>, Al<sub>2</sub>O<sub>3</sub>/Ca(IO<sub>3</sub>)<sub>2</sub>, TiO<sub>2</sub>/Ca(IO<sub>3</sub>)<sub>2</sub>. For the above two kinds of mixtures (a and c), the ratios of H<sub>3</sub>BO<sub>3</sub>, Al<sub>2</sub>O<sub>3</sub>, and TiO<sub>2</sub> to Ca(IO<sub>3</sub>)<sub>2</sub> is the same, respectively after taking the oxide shell into consideration.

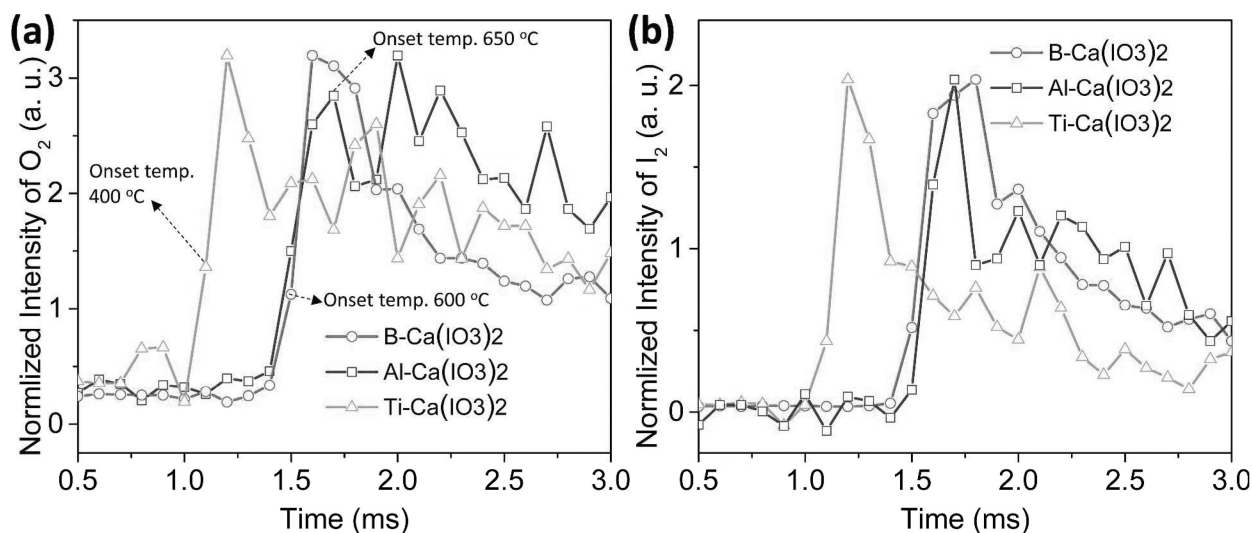


**Figure 6.** Normalized oxygen ( $m/z$ : 32, a) and iodine ( $m/z$ : 254, b) release from  $\text{B}/\text{Ca}(\text{IO}_3)_2$ ,  $\text{Al}/\text{Ca}(\text{IO}_3)_2$  and  $\text{Ti}/\text{Ca}(\text{IO}_3)_2$  composites. The onset temperatures of ignition were also labelled (a).

As mentioned above, compared to pure  $\text{Ca}(\text{IO}_3)_2$ , the decomposition of  $\text{Al}/\text{Ca}(\text{IO}_3)_2$  and  $\text{B}/\text{Ca}(\text{IO}_3)_2$  starts  $\sim 100^\circ\text{C}$  earlier and the decomposition of  $\text{Ti}/\text{Ca}(\text{IO}_3)_2$  begins  $\sim 200^\circ\text{C}$  earlier. The results indicated that all the three metals nanoparticles promote oxidizer decomposition with, Ti nanoparticles being the most efficient. To evaluate the effect of the oxide shell and it is participating in a pre-reaction with the iodate the amount of oxide present in the shells was estimated, mixed with the  $\text{Ca}(\text{IO}_3)_2$ , and its decomposition evaluated by TG/MS. The results shown in Figure 5c and 5d indicate some very minimal obvious effect of the oxide, with  $\text{TiO}_2$  the most facile in promoting the decomposition of  $\text{Ca}(\text{IO}_3)_2$ . The iodine release curves from MS results (Figure 5d) also confirm  $\text{TiO}_2/\text{Ca}(\text{IO}_3)_2$  are the easiest to decompose.

By normalizing the iodine signals ( $m/z=254$ ) to argon ( $m/z=40$ ), the iodine release can be roughly quantified by integrating the area of the peaks (Figure 5b). With  $\text{Ca}(\text{IO}_3)_2$  case as the control baseline, the value of the iodine release peak area from  $\text{Ca}(\text{IO}_3)_2$  is set to 100%. Then the iodine release efficiency of  $\text{Ti}/\text{Ca}(\text{IO}_3)_2$ ,  $\text{Al}/\text{Ca}(\text{IO}_3)_2$  and  $\text{B}/\text{Ca}(\text{IO}_3)_2$  is 79, 87 and 89%. It is also notable that the iodine release from  $\text{Ca}(\text{IO}_3)_2$  and  $\text{Al}/\text{Ca}(\text{IO}_3)_2$  is obvious two-steps process while for  $\text{Ti}/\text{Ca}(\text{IO}_3)_2$  and  $\text{B}/\text{Ca}(\text{IO}_3)_2$  case is a broader one-step release.

The three kinds of  $\text{Ca}(\text{IO}_3)_2$ -based pyrolants were also studied on a fast-heating wire coupled with a time-of-flight MS to investigate the decomposition species. Figure S8 shows the detailed mass spectra, and Figure 6 shows the temporal normalized oxygen ( $\text{O}_2$ ,  $m/z=32$ ) and iodine ( $\text{I}_2$ ,  $m/z=254$ ) release during the 3 ms fast-heating process. From Figure 6, we see clearly that  $\text{Ti}/\text{Ca}(\text{IO}_3)_2$  released oxygen and iodine at a much earlier time ( $\sim 1.0$  ms) and temperature ( $\sim 400^\circ\text{C}$ ), which is consistent with the results of

TG/MS and ignition temperature measurements. It is also notable that for both cases of oxygen (Figure 6a) and iodine release (Figure 6b), the  $\text{B}/\text{Ca}(\text{IO}_3)_2$  has only one major peak while the  $\text{Al}/\text{Ca}(\text{IO}_3)_2$  has at least two peaks, which further confirms that the major decomposition of  $\text{B}/\text{Ca}(\text{IO}_3)_2$  is in one-step. The  $\text{Ti}/\text{Ca}(\text{IO}_3)_2$  also show two peaks of oxygen and iodine release, which is not consistent with the MS result in slow heating (Figure 5b). The second iodine release peak in Figure 5b might be hidden because of the wide first peak. TG/MS results of  $\text{TiO}_2/\text{Ca}(\text{IO}_3)_2$  in Figure 5c and 5d, show a small second decomposition stage and small iodine release peak while the boron case does not.

All three  $\text{Ca}(\text{IO}_3)_2$ -based pyrolants are found to release a large amount of iodine gas as evidenced by iodine vapor release shown in the supporting videos (**Appendix B. supporting videos**). The optical images in Figure S9 also show deposited iodine layer on the top of combustion cell, which further confirm that.

## 4 Conclusion

In this paper, different  $\text{Ca}(\text{IO}_3)_2$ -based pyrolants with iodine content of  $\sim 20$ – $60$  wt-% were prepared and systematically investigated. Three different fuels (B, Al and Ti) were physically mixed with  $\text{Ca}(\text{IO}_3)_2$  with various equivalence ratios from 0.75 to 5.0. The optimal ratio was found to be 2.0 for all the three fuels. The reactivity of the pyrolants can be enhanced by dehydrating the  $\text{Ca}(\text{IO}_3)_2$  or replacing the micron oxidizer particles with submicron particles. The thermal decomposition process of the pyrolants was investigated at low and high heating rate. The results show that B, Al and Ti NPs can promote the decomposition of  $\text{Ca}(\text{IO}_3)_2$ , but the Ti nanoparticles are the most efficient, which lower temper-

ature of the oxygen/iodine release from  $\sim 660^\circ\text{C}$  to  $\sim 400^\circ\text{C}$ . Thus,  $\text{Ti}/\text{Ca}(\text{IO}_3)_2$  has the lowest ignition temperature of  $\sim 400^\circ\text{C}$ . The  $\text{Ca}(\text{IO}_3)_2$ -based pyrolant has a wide range of iodine content ( $\sim 20$ – $60$  wt-%), reactivity ( $\sim 0.1$ – $330$  kPa/ms), burn time ( $\sim 1$ – $165$  ms) and high flame temperature ( $> 2200$  K), which makes it a promising class of biocidal energetic materials.

## Appendix A. Supporting Information

SEM images and XRD characterization of the prepared  $\text{Ca}(\text{IO}_3)_2$ . Detailed formula, SEM images, detailed combustion cell data with flame temperatures of the pyrolants used in this paper. The SEM images and EDS results of  $\text{B}/\text{Ca}(\text{IO}_3)_2$  combustion residue. Schematic showing of T-Jump MS and combustion cell measurement. Detailed T-Jump MS spectrum of  $\text{B}/\text{Ca}(\text{IO}_3)_2$ ,  $\text{Al}/\text{Ca}(\text{IO}_3)_2$  and  $\text{Ti}/\text{Ca}(\text{IO}_3)_2$  composites with sub-micron  $\text{Ca}(\text{IO}_3)_2$  (equivalence ratio is 2.0). Optical image of typical deposited iodine layer after reaction in combustion cell.

## Appendix B. Supporting Videos

The combustion videos (33x slower than real time) in air of 10 mg of  $\text{B}/\text{Ca}(\text{IO}_3)_2$ ,  $\text{Al}/\text{Ca}(\text{IO}_3)_2$  and  $\text{Ti}/\text{Ca}(\text{IO}_3)_2$  composites with large (equivalence ratio of 0.75 and 2.0) and small (equivalence ratio of 2.0)  $\text{Ca}(\text{IO}_3)_2$ .

## Acknowledgments

This work was supported by DTRA. We acknowledge the support of the Maryland Nanocenter and its NispLab. The NispLab is supported in part by the NSF as a MRSEC Shared Experimental Facility. Supporting Information is available online from journal website or from the authors

## References

- [1] G. M. Mancini, J. Revill in *Cyber and Chemical, Biological, Radiological, Nuclear, Explosives Challenges. Terrorism, Security, and Computation*, (Eds.: M. Martellini, A. Malizia), Springer International Publishing, Cham, **2017**, pp. 311–325.
- [2] C. He, G. Zhao, J. P. Hooper, J. N. M. Shreeve, Energy and biocides storage compounds: synthesis and characterization of energetic bridged Bis(triiodoazoles). *Inorg. Chem.* **2017**, *21*, 13547–13552.
- [3] J. C. Oxley, J. L. Smith, M. M. Porter, M. J. Yekel, J. A. Canaria, Potential biocides: iodine-producing pyrotechnics. *Propellants Explos. Pyrotech.* **2017**, *8*, 960–973.
- [4] S. A. Grinshpun, A. A. Adhikari, T. Reponen, E. Dreizin, M. Schoenitz, Neutralization of aerosolized bio-agents by filled nanocomposite materials through thermal and chemical inactivation mechanisms, No. DTRA-TR-16-68, University of Cincinnati Newark United States, 2016 Jun 1st.
- [5] J. M. Shreeve, Energetic materials for bio-agent destruction, No. HDTRA1-11-1-0034, University of Idaho Moscow United States, 2017 Mar 1st.
- [6] S. Cogliati, J. Gabriel Costa, Bacterial spores and its relatives as agents of mass destruction. *J. Bioterror. Biodef.* **2016**, *1*, 1000141.
- [7] Q. Li, G. Korza, P. Setlow, Killing the spores of Bacillus species by molecular iodine. *J. Appl. Microbiol.* **2017**, *1*, 54–64.
- [8] L. C. Brown, Iodine on demand, No. GA-C24040, General atomics report, 2002 Aug.
- [9] H. Wang, J. B. DeLisio, G. Jian, W. Zhou, M. R. Zachariah, Electro spray formation and combustion characteristics of iodine-containing  $\text{Al}/\text{CuO}$  nanothermite microparticles. *Combust. Flame* **2015**, *7*, 2823–2829.
- [10] D. K. Smith, M. N. Bello, D. K. Unruh, M. L. Pantoya, Synthesis and reactive characterization of aluminum iodate hexahydrate crystals  $[\text{Al}(\text{H}_2\text{O})_6](\text{IO}_3)_3(\text{HIO}_3)_2$ . *Combust. Flame* **2017**, *179*, 154–156.
- [11] C. He, J. P. Hooper, J. N. M. Shreeve, Iodine-rich imidazolium iodate and periodate salts: en route to single-based biocidal agents. *Inorg. Chem.* **2016**, *24*, 12844–12850.
- [12] S. Wang, M. Schoenitz, S. A. Grinshpun, M. Yermakov, E. L. Dreizin, Biocidal effectiveness of combustion products of iodine-bearing reactive materials against aerosolized bacterial spores. *J. Aerosol Sci.* **2018**, *116*, 106–115.
- [13] H. Wang, J. B. DeLisio, T. Wu, X. Wang, M. R. Zachariah, One-step solvent-free mechanochemical synthesis of metal iodate fine powders. *Powder Technol.* **2018**, *324*, 62–68.
- [14] S. Wang, X. Liu, M. Schoenitz, E. L. Dreizin, Nanocomposite thermites with calcium iodate oxidizer. *Propellants Explos. Pyrotech.* **2017**, *3*, 284–292.
- [15] X. Liu, M. Schoenitz, E. L. Dreizin, Boron-based reactive materials with high concentrations of iodine as a biocidal additive. *Chem. Eng. J.* **2017**, *325*, 495–501.
- [16] M. A. Hobosyan & K. S. Martirosyan, Iodine pentoxide nanorods for high density energetic materials. *Propellants Explos. Pyrotech.* **2017**, *5*, 506–513.
- [17] T. Wu, A. SyBing, X. Wang, M. R. Zachariah, Aerosol synthesis of phase pure iodine/iodic biocide microparticles. *J. Mater. Res.* **2017**, *4*, 890–896.
- [18] E. M. Hunt, Biocidal energetic materials for the destruction of spore forming bacteria, No. DTRA-TR-13-52, West Texas A&M University, 2015 July.
- [19] C. W. Farley, M. L. Pantoya, M. Losada, S. Chaudhuri, Linking molecular level chemistry to macroscopic combustion behavior for nano-energetic materials with halogen containing oxides. *J. Chem. Phys.* **2013**, *7*, 074701.
- [20] T. Wu, X. Wang, P. Y. Zavalij, J. B. DeLisio, H. Wang, M. R. Zachariah, Performance of iodine oxides/iodic acids as oxidizers in thermite systems. *Combust. Flame* **2018**, *191*, 335–342.
- [21] K. T. Sullivan, N. W. Piekielek, S. Chowdhury, C. Wu, M. R. Zachariah, C. E. Johnson, Ignition and combustion characteristics of nanoscale  $\text{Al}/\text{AgIO}_3$ . *Combust. Sci. Technol.* **2010**, *3*, 285–302.
- [22] H. Wang, G. Jian, W. Zhou, J. B. DeLisio, V. T. Lee, M. R. Zachariah, Metal iodate-based energetic composites and their combustion and biocidal performance. *ACS Appl. Mater. Interfaces* **2015**, *31*, 17363–17370.
- [23] L. Zhou, N. Piekielek, S. Chowdhury, M. R. Zachariah, T-Jump/time-of-flight mass spectrometry for time-resolved analysis of energetic materials. *Rapid Commun. Mass Spectrom.* **2009**, *1*, 194–202.
- [24] H. Wang, G. Jian, G. C. Egan, M. R. Zachariah, Assembly and reactive properties of  $\text{Al}/\text{CuO}$  based nanothermite microparticles. *Combust. Flame* **2014**, *8*, 2203–2208.



- [25] H. Wang, R. J. Jacob, J. B. DeLisio, M. R. Zachariah, Assembly and encapsulation of aluminum NP's within AP/NC matrix and their reactive properties. *Combust. Flame* **2017**, *180*, 175–183.
- [26] G. M. Dutro, R. A. Yetter, G. A. Risha, S. F. Son, The effect of stoichiometry on the combustion behavior of a nanoscale Al/MoO<sub>3</sub> thermite. *Proc. Combust. Inst.* **2009**, *2*, 1921–1928.
- [27] D. Sundaram, Metal-water mixtures for propulsion and energy-conversion applications: recent progress and future directions. *Eurasian Chem. Technol. J.* **2018**, *1*, 53–62.
- [28] S. J. Shitole, Synthesis and characterization of calcium iodate, monohydrate crystals grown in silica gel. *J. Phys. Conf. Ser.* **2013**, *423*, 012060.
- [29] C. Yuan, P. R. Amyotte, M. N. Hossain, C. Li, Minimum ignition temperature of nano and micro Ti powder clouds in the presence of inert nano TiO<sub>2</sub> powder. *J. Hazard. Mater.* **2014**, *275*, 1–9.

Received: February 5, 2018

Accepted: July 19, 2018

Published online: August 30, 2018